



AFRL-OSR-VA-TR-2013-0601

(DCT) MEMRISTIVE MATERIALS AND DEVICES

MAREK SKOWRONSKI

CARNEGIE-MELLON UNIVERSITY

11/19/2013

Final Report

DISTRIBUTION A: Distribution approved for public release.

**AIR FORCE RESEARCH LABORATORY
AF OFFICE OF SCIENTIFIC RESEARCH (AFOSR)/RSE
ARLINGTON, VIRGINIA 22203
AIR FORCE MATERIEL COMMAND**

REPORT DOCUMENTATION PAGE

*Form Approved
OMB No. 0704-0188*

Public reporting burden for this collection of information is estimated to average 1 hour per response, including the time for reviewing instructions, searching existing data sources, gathering and maintaining the data needed, and completing and reviewing this collection of information. Send comments regarding this burden estimate or any other aspect of this collection of information, including suggestions for reducing this burden to Department of Defense, Washington Headquarters Services, Directorate for Information Operations and Reports (0704-0188), 1215 Jefferson Davis Highway, Suite 1204, Arlington, VA 22202-4302. Respondents should be aware that notwithstanding any other provision of law, no person shall be subject to any penalty for failing to comply with a collection of information if it does not display a currently valid OMB control number. **PLEASE DO NOT RETURN YOUR FORM TO THE ABOVE ADDRESS.**

1. REPORT DATE (DD-MM-YYYY) 11/18/2013			2. REPORT TYPE Final		3. DATES COVERED (From - To) 08/01/2010-07/31/2013	
4. TITLE AND SUBTITLE Memristive Materials and Devices			5a. CONTRACT NUMBER FA9550-10-1-0365		5b. GRANT NUMBER	
					5c. PROGRAM ELEMENT NUMBER	
6. AUTHOR(S) Professors Marek Skowronski, Paul Salvador, James Bain			5d. PROJECT NUMBER		5e. TASK NUMBER	
					5f. WORK UNIT NUMBER	
7. PERFORMING ORGANIZATION NAME(S) AND ADDRESS(ES) Carnegie Mellon University 5000 Forbes Avenue, Pittsburgh, PA 15213			8. PERFORMING ORGANIZATION REPORT NUMBER			
9. SPONSORING / MONITORING AGENCY NAME(S) AND ADDRESS(ES) Dr. Gernot Pomrenke AFOSR/RSE 875 North Randolph Street Arlington, VA 22203			10. SPONSOR/MONITOR'S ACRONYM(S)			
			11. SPONSOR/MONITOR'S REPORT NUMBER(S)			
12. DISTRIBUTION / AVAILABILITY STATEMENT						
13. SUPPLEMENTARY NOTES						
14. ABSTRACT CMU proved that the filaments in switching devices do not require any pre-existing inhomogeneities such as dislocations to develop. Instead, the conductive paths form due to intrinsic electronic transport instabilities in oxides. The transfer of electrons present as small polarons in oxides to the high mobility band states has been postulated as the origin of this effect. CMU performed in situ and ex situ electron microscopy analysis of oxide-based memristors and demonstrated that devices can switch without formation of any extended defects including oxygen-deficient secondary phases.						
15. SUBJECT TERMS						
16. SECURITY CLASSIFICATION OF:			17. LIMITATION OF ABSTRACT	18. NUMBER OF PAGES	19a. NAME OF RESPONSIBLE PERSON	
a. REPORT	b. ABSTRACT	c. THIS PAGE			19b. TELEPHONE NUMBER (include area code)	

Final Technical Report

Project title: **Memristive materials and devices**
Performance period: **08/01/2010 - 07/31/2013**
Institution: **Carnegie Mellon University**
PIs: **M. Skowronski, J. A. Bain, and P. A. Salvador**

Summary of major findings and their consequences.

The primary goal of the project "Memristive materials and devices" was identification of mechanisms leading to the electro-formation and resistive switching. Initial experiments of the project demonstrated that the conduction in electro-formed macroscopic metal/oxide/metal devices occurs along a filament with small diameter and results in significant local temperature increase (>200 °C). Contrary to the existing models, CMU proved that the filaments do not require any pre-existing inhomogeneities such as dislocations or pinholes to develop. Instead, the conductive paths form due to intrinsic electronic transport instabilities in amorphous oxides at random locations within the device. The transfer of electrons present as small polarons in oxides to the high mobility band states has been postulated as the origin of this effect. This leads to conductivity increase at high electric field and to current controlled negative differential resistance in part of I-V characteristics.

Carnegie Mellon University performed *in situ* and *ex situ* electron microscopy analysis of oxide-based memristors and demonstrated that devices can switch without formation of any extended defects. Specifically, the devices can switch without nucleation of oxygen-deficient secondary phases. On the other hand, excessive power dissipation in non-optimized structures was shown to lead to plastic deformation, and formation of 2D and 3D defects (Wadsley defects and Magneli phases) in TiO₂. Both types of defects accumulate during repeated switching without forming a well defined filament. They are also prone to large scale (1 μ m) re-distribution during a single switching event. The *in situ* TEM allowed for monitoring the evolution of physical changes in the structure with unprecedented fidelity.

1. Introduction.

The primary objective of the AFOSR project FA9550-10-1-0365 "Memristive materials and devices" monitored by G. S. Pomrenke was the identification of processes underlying all aspects of resistive switching phenomenon. While number of different materials systems exhibit this behavior and several different mechanisms have been proposed [1], of interest to this project was a subset of materials and device structures operating by "valence change mechanism".

The description of the project activities and accomplishments follows roughly the project timeline and focuses on several thrusts. These include:

2. Observation of filament formation in macro devices.
3. Pre-existing inhomogeneities.
4. Effects of local Joule heating
5. Electron transport instabilities.
6. In-situ microscopy.

2. Observation of filament formation in macro devices.

The work on the resistive switching devices initially focused on single crystal materials and devices. The two prototypical systems were Pt/SrTiO₃ Schottky barriers [2] and Pt/SrZrO₃/SrRuO₃ structures [3]. The important observation obtained by the infrared microscopy was that the devices after electro-formation

exhibited filamentary conduction and that the local current flow induced considerable amount of heating [3]. The I-V characteristics of the electro-formation process and the IR image of the Pt/SrZrO₃/SrRuO₃ device under bias is shown in Fig. 1.

During the first quasi-DC sweep, the current of initially high resistance device suddenly increased at -18V indicating the electro-formation. Concomitantly, a bright spot appeared in the IR image. This is fully consistent as dissipation of power in a very small volume of the filament should produce a hot spot due to Joule heating. Additional support for this conclusion, were two I-V curves obtained after the device was cut in half by Focused Ion Beam along horizontal line marked in (Fig. 1(b)). It is apparent that the upper half of the device (the one with the hot spot, marked in Fig. 1(a) as a red line) has a much lower resistance than the lower half (blue line). In all devices tested, there was always one hot spot formed during the electro-formation process. The size of the hot spot in IR images was limited by the diffraction at the 3 micron wavelength used for imaging. Also, the observed temperature excursions (up to 200 °C) were mostly likely limited by the spatial resolution of the system. The real hot spot could be much smaller than observed size and its temperature much higher.

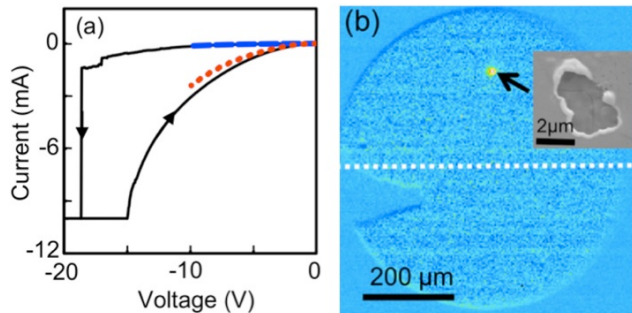


Fig. 1 (a) Electro-forming I-V characteristics (black line) and two I-V lines corresponding to a device which was cut in two. Red line represents the upper half of the device while the blue one the lower half. (b) IR image of the device under bias.

This observation posed two important questions that became to focus of the entire project.

1. Why is only one filament forming? Why do local filaments form at all rather than the entire area of the device being affected? Are there any pre-existing inhomogeneities (pinholes, inclusions, dislocations, etc.) responsible for the local breakdown of the device?
2. Is heating necessary for the filament formation or is it only a byproduct of the filament existence? Can the filament form and device switch with little or not temperature increase?

The answers to both questions are discussed below.

3. Pre-existing inhomogeneities.

One of the early prominent papers on switching was the publication by Szot *et al.* [4]. This group has analyzed lateral memristor devices on single crystals SrTiO₃ and concluded that the electro-formation occurs by diffusion of the oxygen vacancies along cores of pre-existing dislocations. The main argument was observation of straight lines along [100] directions appearing after the electro-formation (Fig. 2). Their appearance was due to increase of absorption associated with the free carriers induced by the reduced cores. The consequence of this model would be that the minimum device size is limited by the density of dislocations in the material.

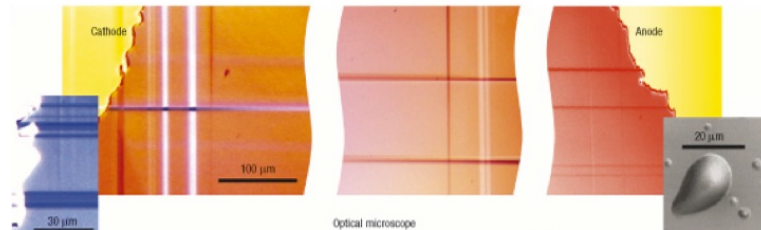


Fig. 2 Optical microscopy image of lines interpreted as diffusion of oxygen vacancies along dislocation lines (Szot et al. Nature Materials **5**, 312 (2006))

Carnegie Mellon University has re-examined this assessment. The devices similar to the devices fabricated by Szot *et al.* after electro-formation indeed exhibited the same cross-hatched pattern of lines. Their visibility in reflection mode over the Pt covered diode area indicates that the lines correspond to surface corrugations rather than optical absorption. AFM scans confirmed this assertion. As shown by the AFM image in Fig. 3(a), the lines appearing on the bare SrTiO_{3-x} surface are steps with step height as tall as 100 nm. The steps gradually decreased in height as a function of distance from the diode area. Strain-stress studies of SrTiO_3 single crystal in literature have also reported such line features and have interpreted them as slip lines resulting from plastic deformation of the crystal [5,6]. Electron channeling contrast imaging (ECCI) performed on the electroforming-induced-lines revealed topographic contrast corresponding to the line features observed by AFM as well as dot features (Fig. 3(b)). Most of the dot features are aligned along the lines. The dot-like contrast in ECCI is typically interpreted as the emergence point of a dislocation inclined at high angle to the surface [7]. The image, therefore, is consistent with an array of dislocations constituting the slip band. In conclusion, the lines were not created by diffusion of vacancies but as the result of plastic deformation during the electro-formation process.

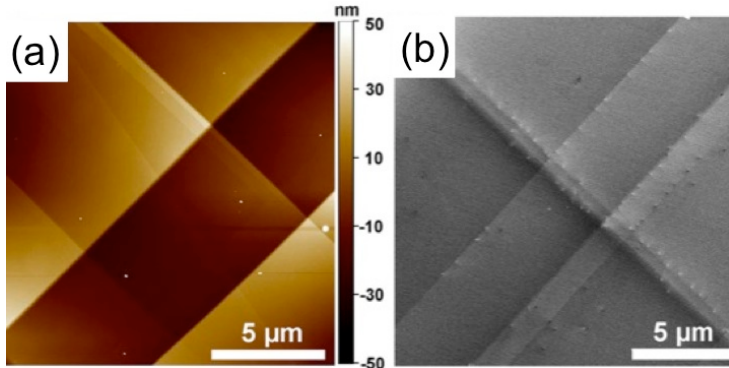


Fig. 3 (a) AFM scan of the Pt diode on single crystal SrTiO_3 after electro-formation. The lines correspond to steps produced by plastic deformation of the material. (b) Electron Channeling Contrast Imaging micrograph of similar diode. The dot contrast along lines is due to individual dislocations.

The cause for the deformation was revealed by the IR microscopy. Fig. 4(a) shows the I-V characteristics of a Pt/ SrTiO_{3-x} Schottky diode. The DC sweeps between -10 and 3 V did not alter the device characteristics. At -13 V, however, the current instantaneously and permanently increased indicating the electro-forming event. Thermographic images of a Pt/ SrTiO_{3-x} diode under bias indicated that Joule heating was significant during electroforming. Figure 4(b) shows the temperature distribution of the diode at the bias close to electroforming voltage. The grey area in the center of the diode was above the detection limit of the Infrascope (on Pt $T_{\text{limit}}=221$ °C). Coincidence of the area with high temperatures in Fig. 4(b) with the location of cross-hatched lines in Fig. 3 indicate that the deformation was caused by the thermal stresses induced by local heating.

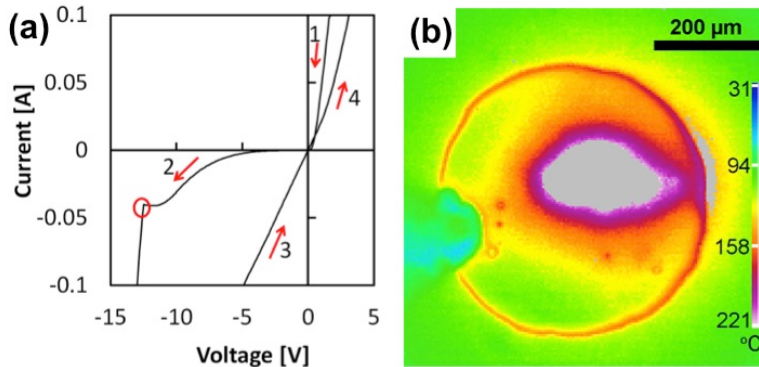


Fig. 4 (a) I-V characteristic of the Pt/ SrTiO_{3-x} Schottky diode with the numbered arrows indicating the voltage sweep direction. (b) Thermography image of Pt/ SrTiO_{3-x} at -15 V during electroforming.

The above conclusion does not exclude the possibility of the pre-existing extended defects being

necessary as the nucleation site for the filament. This possibility was elucidated on lateral micron and submicron memristor structures on single crystal SrTiO_3 [8]. The approach used by CMU relied on fabrication of memristor structures on heavily dislocated and dislocation-free areas of a bulk SrTiO_3 . The initial distribution of dislocations in the substrate was mapped out using Electron Channeling Contrast Imaging method and the test structures were fabricated in low dislocation density areas in ECCI images. The results are summarized in Fig. 5 and 6.

Fig. 5(a) shows the ECCI image of as-fabricated lateral PT electrodes on single crystal substrate. The two large white areas on both sides are Pt contact pads which are isolated from the SrTiO_3 by a layer of SiO_2 . The only contact with the SrTiO_3 was formed by small rectangular electrodes protruding from the contact pads. The grey area in the middle is the exposed SrTiO_3 with the weak point-like contrast corresponding to dislocations intersecting the surface. Clearly, many dislocations were present in the active area of the device. The middle figure depicts the same area after the device was electroformed and switched repeatedly. The metal electrodes were stripped with an aqua regia etch leaving an outline of the electrodes. The etch is selective attacking the dislocations producing dislocation etch pits visible in the image. Their number at position corresponds to the dislocations in the ECCI image. Fig. 5(c) shows the electro-forming and switching I-V characteristics. Fig. 6 shows corresponding images obtained on the device fabricated in the dislocation-free area. As is apparent in Fig. 6(c), the closest dislocation to the device was about 10 microns away from the active area. The I-V characteristics of both devices, however, are virtually the same with similar forming and switching voltages and currents. This constitutes a very direct argument that dislocations do not matter in electro-forming and switching. Also, since the ECCI is sensitive to any source of strains, the images would detect any extended defects appearing in the electro-formation process. Absence of such contrast questions the commonly accepted model of switching being due to formation of secondary phases [9,10].

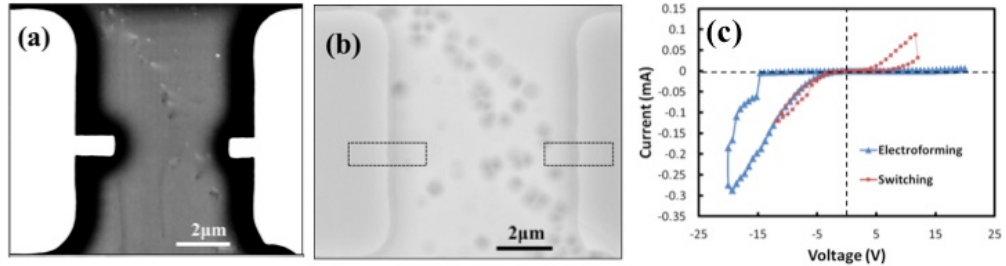


Fig. 5 (a) Electron Channeling Contrast Imaging micrograph of device before electroforming showing pre-existing dislocations in the gap between electrodes. (b) Secondary electron image of the same device after electroforming, switching and removal of electrodes by etching in aqua regia. Dotted line indicates the location of the electrodes that were removed during the etching process. (c) I-V characteristics corresponding to electroforming and switching.

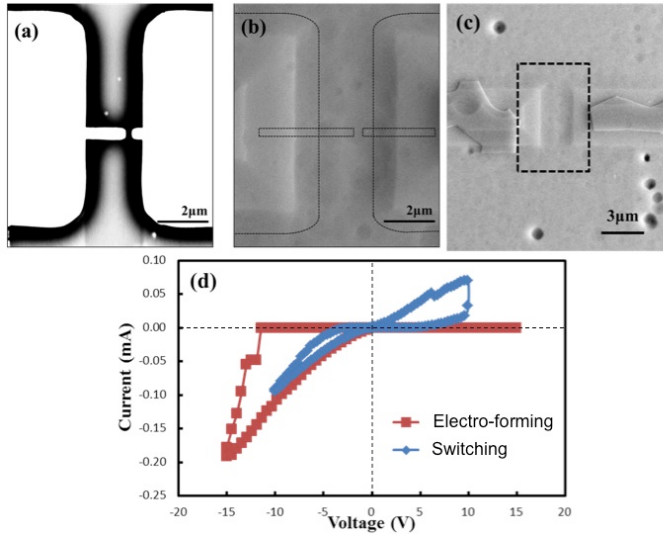


Fig. 6 (a) ECCI micrograph of device before forming showing no pre-existing dislocations. (b) Secondary electron imaging of the same device after electroforming, switching and removal of electrodes by etching in aqua regia. (c) Lower magnification SEM image showing the nearest dislocation etch pit to be 10 μm from the device. Dashed line marks the area shown in (a) and (b). (d) I-V electroforming and switching characteristics.

The conclusion of this section is that extended defects can be formed during electro-formation and /or switching but are not necessary for the formation of the conductive filament in lateral structures. The devices that have been formed and switched do not have to contain any extended defects.

4. Effects of local Joule heating.

One of the effects of local Joule heating are the changes of the electrode and functional layer microstructure. Number of physical changes in memristors has been reported by several groups. The most commonly observed effects are the changes of the top metal electrode referred to as de-wetting, formation of bubbles, or local melting. The size of the affected area is typically several microns [3,9,11,12]. Reported changes within the functional layer include crystallization [10,13,14] and formation of oxygen deficient phases [9,10,14,15]. What is not clear is if the reported changes are necessary for the commonly fabricated vertical devices to function or are they an artifact associated for example with local Joule heating. For example, the changes in top electrode morphology were interpreted as due to oxygen loss from the functional layer [11]. It could also be an artifact of local heating that occurs due to the current increase after forming.

Carnegie Mellon University has optimized the TiO₂-based device design and electroforming procedure in order to minimize the power dissipated during forming and switching. The optimized structures consisted of Pt(15nm) / TiO₂(20nm) / Pt(15nm) / Ti(5nm) / Si(substrate). The 5 nm thick Ti adhesion layer and the 15 nm thick Pt bottom electrode were deposited as blanket layers on a Si wafer by DC sputtering at room temperature. The TiO₂ layer was sputtered from a TiO₂ ceramic target in a RF sputtering system. In addition to optimizing the structures, CMU has improved the control of electro-forming process. The typical approach to limiting the power dissipation during electro-forming is to use a current compliance on the source-meter. The slow reaction time of the instrument results in a current spike when the resistance of the DUT suddenly drops. Also, the BNC cables have a capacitance high enough that their discharge can damage the device. CMU has eliminated these artifacts using a series resistor close the DUT (Fig. 7) [16].

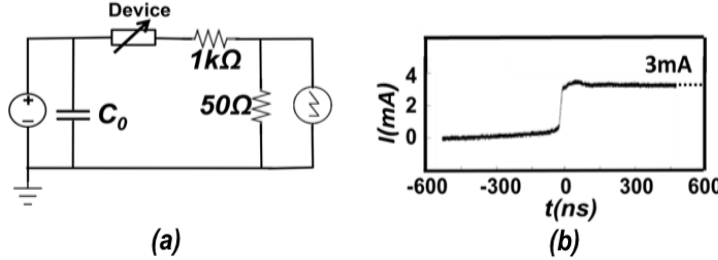


Fig. 7 (a) Circuit schematics of forming with an external resistor connected close to the device. (b) Transient current measured at forming. There is no current overshoot during forming.

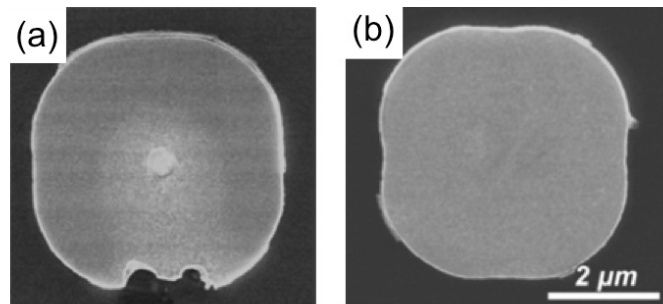


Fig. 8 SEM images of identical devices after forming with different methods: (a) 1 mA compliance only, and (b) external resistor next to the device.

The changes within the functional oxide layer has been assessed by Transmission Electron Microscopy [17]. The devices had 200 nm-size square top electrodes patterned by e-beam lithography. The small size of the device allowed for an easy positioning of the FIB cut for TEM sample preparation. The SEM top-view and TEM cross-sectional images of the control as-fabricated device are shown in Fig. 9. Granular contrast features with characteristic sizes between 3 and 10 nm is seen on the Pt surface, likely due to the polycrystalline grains in the sputtered metal. Figure 9(b) shows a bright-field TEM image of the device in cross-section. The 4 layers of the structure can be distinguished. Moving from the bottom to the top in the image, the grey area in the lower part of the image corresponds to the silicon substrate, followed by a thin layer of titanium, dark contrast associated with the Pt bottom electrode, a grey functional TiO_2 layer and the top Pt patterned electrode. The granular contrast above the top electrode is a protective Pt layer deposited during focused ion beam (FIB) sample preparation. The interface roughness between the top electrode and the oxide layer is below 2 nm. The TiO_2 layer appears featureless without any sign of lattice fringes or polycrystalline grains. The top electrode, however, shows weak contrast of grains with a characteristic size of about 5 nm, which can be considered to be in agreement with the SEM image. (The size is difficult to assess precisely in the TEM image as the grain diameter is smaller than the foil thickness and the grain images overlap.)

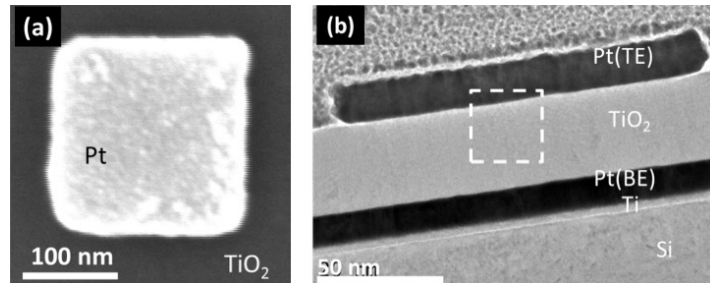


Fig. 9 (a) SEM image of a resistive switching device with patterned 200 nm Pt top electrode. (b) Bright field cross-sectional TEM image of the Pt / TiO_2 / Pt / Ti device. Dashed square marks a region analyzed by HR-TEM below.

After electroforming process in which the dissipated power was about 0.5 mW, the top electrode stayed largely in the original square shape with signs of the morphology change only in the upper left corner (Fig. 10). The upper half of the electrode shows granular features with 30-50 nm size, almost one order of magnitude bigger than their original size. The upper left corner of the electrode appears to have experienced deformation with some of the electrode having been ‘blown off’ and likely landed as a separate piece on the top right corner. The morphology change of the metal is consistent with a roughly circular area of change centered in the upper left corner of the device with a diameter of 80 nm. Figure 10(b) shows a cross-sectional bright-field TEM image taken through the upper half of the electrode, as indicated by the rectangle in (b). Diffraction contrast is clearly visible within the TiO_2 layer in the location corresponding to the affected morphology. Based on these observations, we argue that the electroformation induced crystallization of the oxide layer in the upper left corner of the device only while the entire top electrode experienced grain growth. It appears that the upper left corner was the location of the filament and of highest temperature increase.

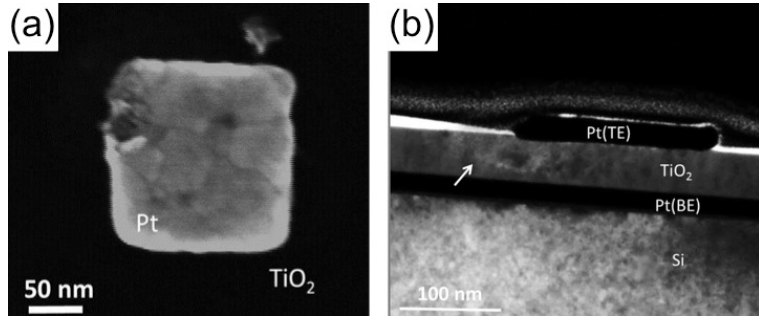


Fig. 10 Images of electroformed-only device: (a) and (b) top-view SEM image. (c) TEM cross-sectional image. Arrow indicates contrast change in the TiO_2 layer.

The results of thermal modeling of the electro-formation process are shown in Fig. 11. The material parameters for Pt, Ti, TiO_2 , and Si have been extracted from the literature with all dimensions corresponding to the device design. The dissipated power (0.5 mW) was measured during electro-formation of the device. The simulation was performed for four values of the conducting filament diameter: 10, 50, 100 and 200 nm (only 50 and 200 are shown in the figure).

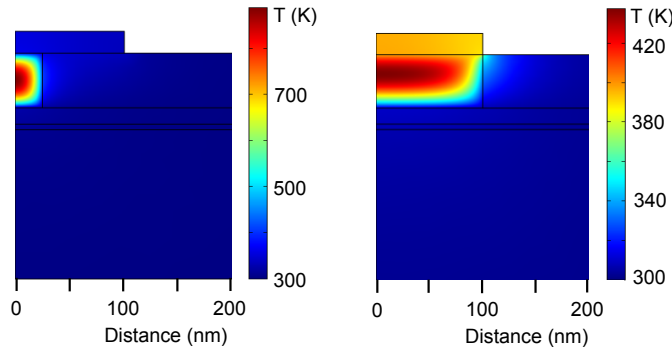


Fig. 11 Simulation of temperature distribution in 200 nm Pt/ TiO_2 /Pt/Ti/Si memristor with power dissipation of 0.5 mW. (a) Assuming conducting filament with 50 nm diameter and (b) 200 nm diameter.

Several conclusions are immediately apparent. The metal electrodes act as efficient heat spreaders and do not heat up unless the diameter of the filament approaches the lateral size of the electrode. Significant temperature increase within the oxide is confined to the volume of the filament. Based on these two characteristics, we can state that the filament in investigated devices had a diameter of about 200 nm. The absolute temperature increases of the top electrode and within the functional layer are about 100 °C and 150 °C and appears too low for the observed changes in the morphology. These values could have been underestimated by neglecting the thermal resistivity of the Pt/ TiO_2 interface. CMU will determine this and other relevant material parameters experimentally and will implement a detailed thermal model of switching devices.

Similar morphology changes were observed in devices which were both electroformed and switched. An example is shown in Fig. 12 (the device was on the same die and nominally identical to those shown in Fig. 9 and Fig. 10). Although similar, further electrical stressing from the switching cycles produces more extensive changes. Figure 12(a) shows that the top electrode has recrystallized and deformed. One can also notice the appearance of a pinhole in the electrode. Formation of pinholes has been reported in Pt polycrystalline layers annealed for 30 min above 650°C and this provides lower bound of the device temperature. This is in agreement with the simulation of the temperature distribution which indicates that the temperature of the top electrode exceeded 500 °C and that in the oxide layer exceeded 700 °C (Fig. 13). In a cross-sectional TEM image taken from the same sample (Figure 12(b)), it is observed that almost all of the TiO₂ film under the electrode exhibits strong diffraction contrast. The comparison between Fig. 8 and Fig. 10 suggests that they experienced the same type of physical changes, such as Pt grain growth and TiO₂ crystallization, but different in extent. Along with the crystallization effect, the interface between the top electrode and the oxide layer has roughened significantly compared to both the pristine and the electroformed-only device. Greater TiO₂ crystallization is a logical consequence considering the higher maximum dissipated power (~2.8mW) at RESET was seven times higher compared to electroformation (~0.4mW).

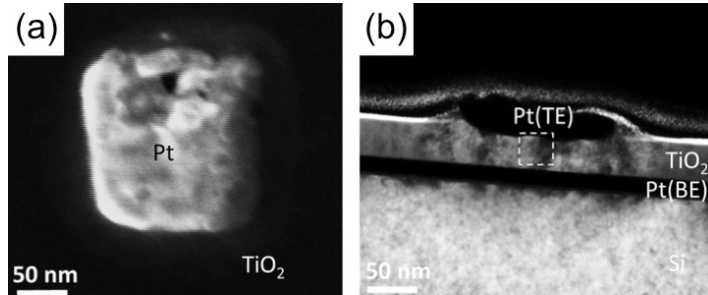


Fig. 12 (a) and (b) SEM images of the electroformed and switched 200 nm memristor. (c) TEM bright field image of the sample milled at the location shown in (b) by the dashed rectangle.

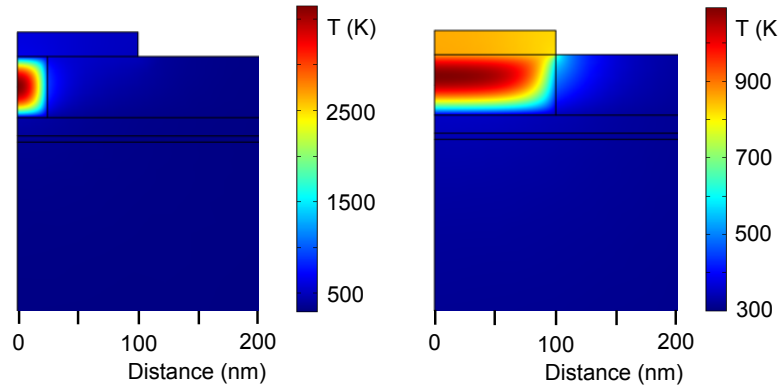


Fig. 13 Simulation of temperature distribution in 200 nm Pt/TiO₂/Pt/Ti/Si memristor with power dissipation of 2.8 mW. (a) Assuming conducting filament with 50 nm diameter and (b) 200 nm diameter.

In order to understand the exact nature of the crystallized film, CMU conducted high-resolution (HR) TEM of the TiO₂ layer in the as-fabricated device (Fig. 14(a)) and the switched one (Fig. 14(b)). Insets in Fig. 14 show the Fast Fourier Transform (FFT) of the corresponding HRTEM image. The TiO₂ film in (a) is amorphous as it shows no phase contrast (lattice fringes) in the original image and few, poorly defined peaks in the FFT image. The formed-and-switched device, on the other hand, shows clear lattice fringes with various orientations, and the corresponding FFT image shows multiple peaks indicating local atomic periodicity. The largest lattice spacing measured in Fig 14(b) is 3.5~3.6 Å, which could correspond with anatase (101) planes. Such planes have the largest atomic spacing for all known diffracting planes in the three naturally occurring stoichiometric TiO₂ crystals: rutile, anatase and brookite. Therefore, the measured lattice fringes can be considered a signature of the anatase phase. An amorphous to anatase

transformation of TiO_2 is reported to happen above 300°C. In addition to layer crystallization, Kwon *et al.*⁹ and Strachan *et al.*¹⁰ reported observation of crystalline oxygen-deficient phases in TiO_2 -based memristors and suggested that the oxygen loss is responsible for the switching effect. Our TEM analysis shows only very limited crystallization, much below that observed in Samsung and HP devices. We do not see any indication of the appearance of Magneli phases (oxygen deficiency). The difference in behavior could be due to much lower power dissipation in CMU devices. In other words, the Magneli phases can form in TiO_2 memristors but their presence is not required for switching.

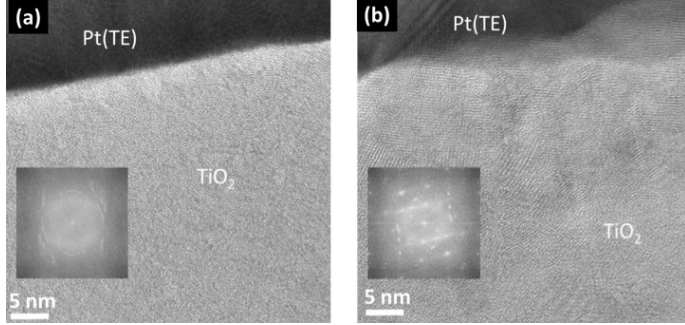


Fig. 14 Comparison of high resolution TEM images from: (a) a pristine TiO_2 film as given in Fig. 9; (b) the electroformed and switched device as given in Fig. 12. The TEM-FFT patterns of the TiO_2 layer are shown in insets.

Independently of the changes in the microstructure of the devices induced by Joule heating, one can expect significant change in the rate of thermally activated processes. One of them is the oxygen vacancy diffusion which is frequently invoked in the formation of the filament [1,18] and switching [10]. The data on the vacancy diffusion have been available only at high temperatures. CMU has assessed the oxygen vacancy motion in conditions and structures very similar to the operating conditions of memristive devices [2]. The test structure were the Pt/ SrTiO_3 Schottky diodes fabricated on single crystal substrates intentionally doped with oxygen vacancies by annealing. Fig. 15 shows CV characteristics of two Schottky diodes on niobium- and vacancy-doped SrTiO_3 . The Nb: SrTiO_3 diode has a perfectly linear CV characteristics indicating uniform doping density in the subsurface region. The SrTiO_{3-x} exhibits a slope that's increasing at lower voltages. This type of characteristics is due to a decreasing charge density as one approaches the surface. A likely interpretation of this effect is the oxygen slowly diffusing into the bulk SrTiO_3 from the Pt electrode.

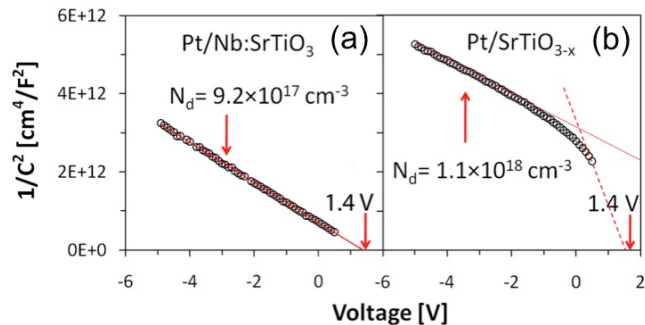


Fig. 15 C-V profiles of (a) Pt/Nb: SrTiO_3 Schottky diode and (b) Pt/ SrTiO_{3-x} Schottky. The change of slope at low voltages indicates surface depletion of vacancies.

This assertion was tested by repeatedly performing the CV scans and monitoring changes in donor density as a function of time. Fig. 16(a) shows the evolution of vacancies without applied bias. In the built-in field, the vacancies are expected to drift toward and accumulate next to the metal electrode. This part of the subsurface region is inaccessible to the CV technique. The accumulation is accompanied by a decreasing vacancy density deeper in the crystal. The shift is almost linear with time. Similar but faster drift is observed under applied reverse bias (Fig. 16(b)). We have estimated the vacancy mobility at $1.5 \times 10^{-13} \text{ cm}^2/\text{Vs}$. This value is about eight orders of magnitude too low to explain the switching times in the 10 ns range. The most likely resolution of this problem is the local Joule heating. Assuming the diffusion coefficient activation energy of 1 eV, the increase of the temperature by 300 oC would speed up the diffusion by about 10^8 .

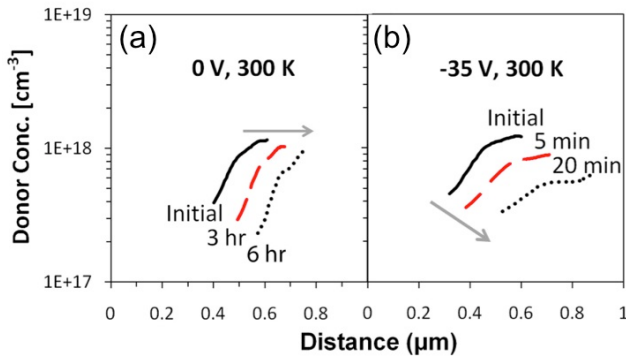


Fig. 16 Charge density as a function of voltage and time in Pt/SrTiO_{3-x} Schottky diode. (a) Diode with no bias and (b) -35V reverse voltage.

In summary, local Joule heating appears to be necessary for fast switching. It also frequently results in changes of the material microstructure including crystallization and grain growth in metal electrodes. However, the appearance of oxygen deficient Magneli phases was not observed and, in agreement with the previous section, not necessary for switching.

5. Electron transport instabilities.

As concluded above, the conducting filament can form without any apparent pre-existing inhomogeneity. This poses the question on the nature of instability that leads to the formation of a local breakdown. We argue below that the answer is rooted in the electronic transport characteristics of the memristive structures. The experiments described below were performed on devices fabricated on sputtered TiO₂, Ta₂O₅, and/or HfO₂ thin films with Pt electrodes. The results were submitted and are under review by Nature Nanotechnology.

Figure 17 shows four quasi-DC *I-V* characteristics obtained from a single crossbar-type Pt/Ta₂O₅/Pt device. The four curves were obtained using different values of series resistor, R_s (the circuit schematic is shown in Fig. 17(b)). The measurements were made by sweeping the source voltage while measuring the voltage across the device only (V_m in the figure). The black line corresponds to the *I-V* obtained with small series resistance ($R_s = 100 \Omega$). The current initially increases super-linearly and then at 5.75 V snaps back (electroforms) leaving the device in the low resistance ON state. The electro-formation event is effectively instantaneous (marked by the dashed black line in the figure) on the time scale of the source-meter response. No intermediate states could be recorded.

The remaining curves (collected beforehand) do not show a permanent change and can be retraced for decreasing source voltage. The red curve was obtained with $R_s = 34 \text{ kW}$. At low voltages, it follows the same path as the one for $R_s = 100 \Omega$ but extends to higher current values without forming. At about 6 V, the *I-V* trace gradually bends back forming a part of an S-type curve characteristic of current-controlled negative differential resistance (CC-NDR). The presence of CC-NDR usually indicates the presence of an instability that leads to the spontaneous formation of high current density filaments within the device [19,20]. This phenomenon is characteristic of nonlinear dynamic systems, often referred to as *bifurcation*. The presence of CCNDR also implies that the system will 'snap' to a low resistance state (in this case, forming) if a low source resistance is used. However, with large source resistance, the shallow slope of the load-line would prevent such 'snap' and instead show the complete device *I-V* as demonstrated by red, blue, and brown traces.

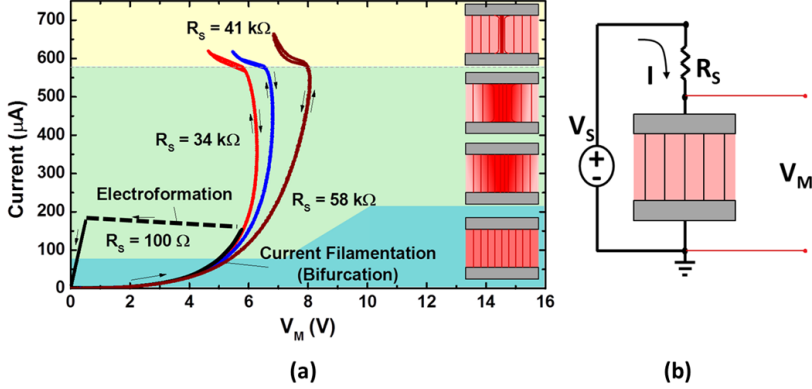


Fig. 17 Negative differential resistance I-V (NDR) in $\text{Ta}_2\text{O}_{5-x}$. **(a)** Electroformation with a ‘snap’ observed in samples with 100Ω series resistance (black trace). This is prevented by using a large source resistance (red, blue and brown traces). Current filamentation causes the device I - V to deviate from each other due to bifurcation. **(b)** Circuit schematic shows the experimental setup with V_M representing the device voltage.

The I - V traces obtained with even higher R_s deviate from the red trace and from each other. This observation is in agreement with suggested current filamentation, as the divergence of these curves measured across the same electrical terminals must have its origin in different physical states of the device. In the case of filament formation, the difference is the diameter of the filament. In other words, the R_s defines the I - V path of the device post-bifurcation. While the data in Fig. 17 were obtained on $\text{Ta}_2\text{O}_{5-x}$ -based devices, we have observed similar behavior in other switching oxides such as TiO_{2-x} and HfO_2 .

Additional insight into the dynamics of the electro-formation process and current filamentation was obtained using time domain transmissometry. It uses constant voltage pulses applied across the device and a 100Ω resistor connected in series. TDT allows for monitoring the change of voltage across the device and current as a function of time. Identical devices can be formed at a wide range of voltages, with lower voltages requiring longer incubation time before the device undergoes the electro-formation [21,22]. Fig. 18(a) shows the voltage across the device as a function of time. Each curve corresponds to the trace during a different voltage pulse, applied to the same device. Each pulse had the same amplitude but different duration, allowing for the interruption of the process at different stages. The initial decrease of voltage (initial negative slope) is associated with decrease of device resistance due to Joule heating. This part of the transient can be simulated using known materials parameters and assuming uniform current flow. The bump at 38 ns is due to a parasitic pulse reflection in the system while the rapid drop between 45 and 55 ns corresponds to the beginning of the electro-formation process. We assert this based on the magnitude of the resistance change. For example, the device resistance during pulse 4 (green curve in Fig. 18(a)) at the onset of the rapid drop is $5 \text{ k}\Omega$ and the resistance value at the point of pulse termination is 250Ω . This change is too big to be explained by thermal effects. Moreover, while there was no permanent change of the device resistance after pulses 1-3 terminating before the completion of the process, the device was formed after the pulse 4. The resistance did not recover and remained at the 250Ω level after the pulse. The conclusion here is that the rapid drop in resistance in Fig. 18(a) does correspond to the electro-formation process. The initial part of the process is volatile and therefore has to be electronic in nature rather than one involving atomic motion.

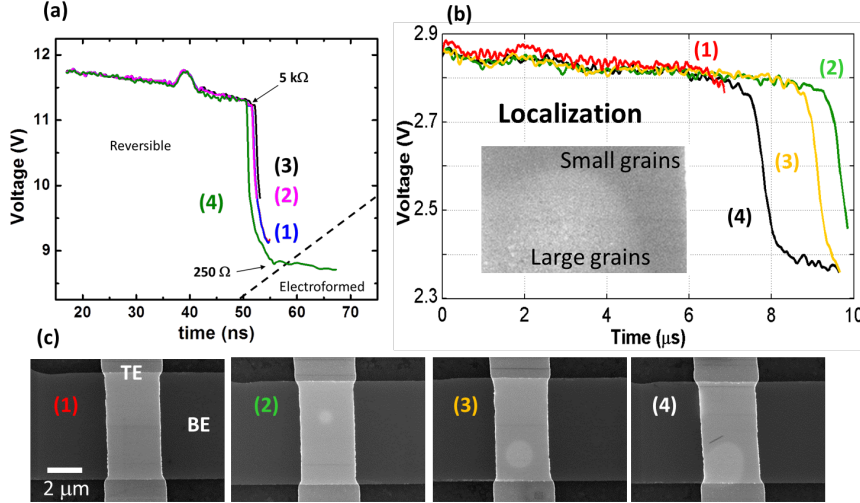


Fig. 18 Pulsed electroforming experiments. (a) Voltage dynamics obtained by pulsing the device repeatedly (1 through 4) with increasing pulse duration for the same $\text{Ta}_2\text{O}_{5-x}$ device. Large resistance change observed without any permanent change until pulse 4 (b) Similar pulse reversibility experiments on TiO_{2-x} show morphological changes (shown in (c)) due to higher power dissipation compared to $\text{Ta}_2\text{O}_{5-x}$.

The results of the similar experiment performed on TiO_{2-x} devices are presented in Fig. 18(b). Each voltage transient and the corresponding Scanning Electron Microscopy (SEM) image were collected on a different but nominally identical device and each device was exposed to only one pulse. The images show the cross bar-type devices with the light grey vertical strip corresponding to the top electrode and the horizontal darker grey strip corresponding to the bottom electrode. The active area of the devices is the rectangle at the intersection of the electrodes. As in Fig. 18(a), the pulses were interrupted at various stages of the electro-formation process. Traces 1-3 correspond to devices that retained their original resistance after the pulse while trace 4 corresponds to the device on which the electro-formation was completed with the permanent drop of resistance. The red trace (1) corresponds to the process interrupted during the uniform current flow stage. The SEM image obtained after this single pulse shows perfectly uniform contrast over the active part of the device. SEM image obtained on the device which experienced the first part of rapid decrease of voltage (trace 2 in Fig. 18(b) and image 2 in (c)) shows a bright round feature with diameter of 1.5 μ m on the top electrode.

High magnification SEM images indicate that such contrast change is the result of grain growth of the platinum that constitutes the top electrode (inset in Fig. 18(b)). At the center of some halos produced by electro-formation at higher voltages (not shown), the electrode either delaminated and/or melted exposing the oxide layer. This behavior was reported by several groups on TiO_{2-x} devices [9,12]. The morphological changes in Pt electrode occur due to localized current flow within the functional layer and consequent large temperature excursions. The size of the halo on the device which experienced larger resistance decrease (trace 3) increased to 2 μ m eventually attaining diameter of 3 μ m on the device with permanent resistance change. Such morphological changes on the top electrode are not seen on $\text{Ta}_2\text{O}_{5-x}$ devices apparently as a result of lower temperature excursions. This observation is a direct evidence of current filamentation occurring before any permanent changes (such as vacancy accumulation) take place in the memristive devices. This instability is reversible and electronic in nature. Only at its later stages and after the core of the filament reaches high temperatures due to high current density, do the physical changes in the device structure take place.

The negative differential resistance is caused by the dependence of conductivity of the device on applied voltage. In systems where the conductivity decreases at higher voltages, one can expect formation of high electric field domains perpendicular to the applied field. This leads to Voltage Controlled NDR and can produce as its consequence Gunn effect (voltage and current oscillations under DC bias). The increase of conductivity with the field, leads to Current Controlled NDR and formation of high current density filaments parallel to the applied field [20]. There are numerous mechanisms that can lead to CCNDR with

one of them being Joule heating [23,24]. In many materials, increase of temperature results in increase of carrier density and as a consequence higher conductivity. This clearly is the case for many functional oxides used in memristive devices. We have, therefore, attempted to determine if the origin of CCNDR in memristors is purely of thermal origin or does it have an electronic component.

Figure 19(a) shows three I - V characteristics: the black and red traces are DC I - V with $R_S = 100 \Omega$ and $34 \text{ k}\Omega$, respectively, as shown in Fig. 17(a). Since the sweep rate is low, the devices reached thermal steady state at every point (i.e. they heated up). The points on the blue curve were obtained in a pulsed experiment where the current and voltage across the device was measured 1 ns after the pulse's leading edge. Since the thermal time constant of our devices is about $2.5 \mu\text{s}$ [22], one can assume that the temperature of the device remained at the stage temperature. It is apparent that excluding the self-heating (blue curve) extended the range of voltages that could be reached without device forming and reduced the current at any given voltage eliminating the CC-NDR. In addition to three I - V curves, Fig. 19(a) also shows the results of another series of pulsed I - V experiments represented by almost vertical violet lines. The pulse duration in this experiment was always $5 \mu\text{s}$ and the two points at the ends of the lines correspond to voltage and current reading at 1 ns and 5 μs . During the pulse, the temperature of the device evolves, approaching the steady state at 5 μs . The coincidence of the end points in this experiment and the black trace (DC with the same load resistor) confirm that filamentation and CC-NDR in the low voltage/current range is purely a thermal phenomenon in our devices. In other words NDR appears because the device becomes more conductive as it carries more current because of self-heating.

While we have argued that CC-NDR indicates current filamentation, it is not clear, at which specific voltage along the CCNDR characteristics does the filament form. We can estimate this by analysis of the dependence of device temperature on dissipated power. For the sake of discussion, let us assume that the current flow is uniform for the entire I - V curve obtained with $R_S = 34 \text{ k}\Omega$ (Fig. 17(a)). The device temperature at every voltage was extracted from the pulsed I - V measurement calibration as a function of stage temperature, shown in Fig. 19(b). This data maps the non-linear dependence of current on voltage and temperature and allows the device resistance itself to serve as a thermometer. In Fig. 19(c), we use this thermometry technique to plot the rise in steady-state temperature due to Joule heating during the DC voltage sweep as a function of power dissipated in the device (red trace). The expected rise in temperature should depend linearly on power:

$$\Delta T = \frac{1}{k_{th}} \frac{t}{A} P \quad (1)$$

where, ΔT is the rise in temperature in Kelvin, k_{th} is the thermal conductivity of the materials leading to the thermal ground, t is the distance the heat travels to thermal ground, A is the area of the current filament, and P is the power dissipated at the heat source.

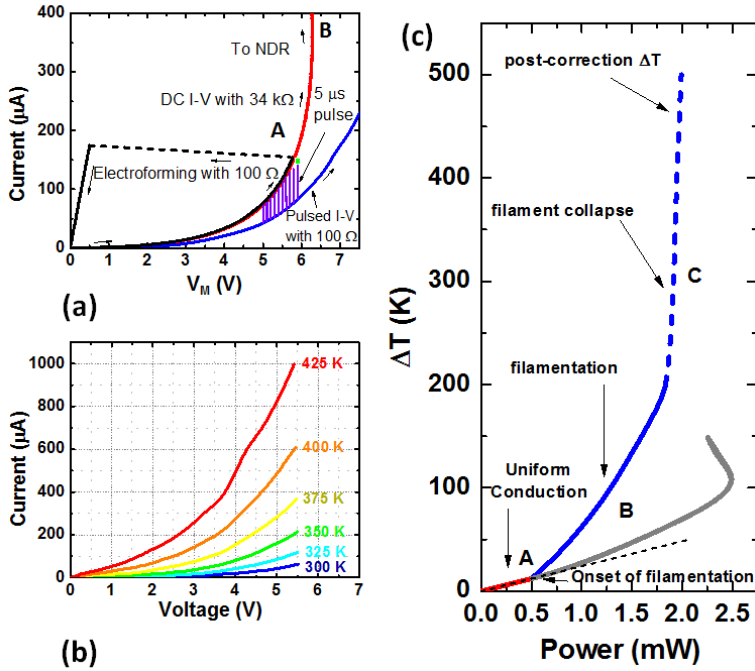


Fig. 19 Temperature and voltage nonlinearities as the origin of filamentation. (a) Adiabatic pulsed I - V (blue trace) without self-heating. The violet I - V dynamic curves connect the initial and the final I vs. t and V vs. t points at 1 ns and 5 μ s. Electroformation occurs in the 5 μ s long pulses at the same V , I combination (green spot) as the DC case (black). (b) Adiabatic pulsed I - V curve taken as a function of temperature with non-linearities in both temperature and voltage. (c) ΔT vs. P obtained by applying thermometry to the DC I - V taken with a 32 k Ω resistor in series (red, gray curve). Blue curve shows the corrected local temperature. Non-uniform conduction sets in at point A due to thermal non-linearity. Region B represents the thermal filamentation followed by a sharp collapse of the filament due to field/current density dependent instability (Region C).

At low voltages, the current flow is uniform and A corresponds to the area of the device. This gives the constant slope of 0.025 K/mW in Fig. 19(c)). This slope corresponds to thermal resistance which is consistent with the thermal resistance felt by a uniformly conducting 5 μ m square device deposited on 1 μ m thick SiO₂. At 600 mW, the $\Delta T(P)$ slope increases indicating the onset of current constriction (point A in the DC I - V curves). The subsequent section of the curve is gray (at powers above 600 mW) to indicate that the temperature calibration is no longer correct when filamentation sets in; the gray section can only be taken to be a lower bound on the device temperature. As the bias increases further past the onset of filamentation, the slope continues to increase indicating gradual reduction of the filament diameter. The deviation from the initial slope up to 2 mW is attributed to thermally-induced CC-NDR. Following this, a steep change of slope occurs at higher powers indicating that the mechanism of the non-linearity is completely different from the one that occurs at point A. This region corresponds to the collapse of the filament resulting into a very localized current flow, which we refer to as the electronic filamentation (making a distinction in the non-linearities). One can also estimate the true temperature by calculating a self-consistent solution for a filament size under the constraints of simultaneously satisfying the adiabatic I - V - T relationship (Fig. 19(b) with extrapolation as necessary) and the thermal resistance experienced by the same filament size. This gives the blue trace. It must be noted that the entire NDR curve (up to point C) is reversible and hence we assert the nature of this localization to be electro-thermal and preceding the motion of atoms or vacancies. Moreover, such deviation is also seen in dynamics measurements.

We have presented the experimental evidence of electronic instability in oxide materials commonly used in fabrication of memristive devices. During the approach to the instability, the temperature gradually increases linearly with power to about 320 K. At this point the current flow constricts and the actual temperature of the filament increases faster than uniform current flow calibration. For the Pt/Ta₂O_{5-x}/Pt device discussed in this work, the steady temperature reaches ~500 K as the extracted filament diameter reduces from 5 μ m (uniform conduction) to 1 μ m due to thermal NDR. Additional power produces further filament collapse, and temperature increases rapidly, reasonably estimated as high as 1000 K as the filament diameter collapses to ~10 nm (same as reported by Kwon *et al.* [9]). These temperatures provide sufficient activation energy to change the oxide in the different ways reported in literature – cause oxygen vacancy creation, crystallization, secondary phase formation and/or melting of the top electrode. The

proposed mechanism explains these changes and removes the inconsistency in explaining reduction of the oxide at low temperature. It parallels the mechanism that has been widely accepted in chalcogenide glasses and referred to as "threshold switching" [25,26].

The CC-NDR in metal/oxide/metal structures have been reported number of times in the literature [27-29]. Most observations have been made on electroformed devices that already contained a permanent conducting filament. This clearly is only remotely relevant to the discussion of the electroformation process presented here. The model presented in the paper and its experimental evidence agrees with the simulation of the *I-V* characteristics reported by Alexandrov *et al.* [30]. The CC-NDR is caused by increase of the conductivity with temperature and electric field. One could, therefore, pose the question what specific phenomenon is responsible for the increase of conductivity. Among many possibilities the one that would explain most of the experimental data is the small polaron hopping.

There are two solutions for the Schrodinger equation describing electron in deformable solid [31,32]. One is the extended state known as the band electron. Such state is typically characterized by high mobilities in the 10-100,000 cm²/Vs range. The other possible state referred to as a polaron corresponds to a localized electron with the wavefunction sometimes localized to with one unit cell (small polaron). The extra charge results in displacement of ions around the electron and much lower mobilities. Small polarons move by hopping between neighboring equivalent sites [33]. In some materials, such as crystalline TiO₂, the two forms can co-exist [34], both contributing to conductivity. It is possible to envision a process by which the predominant carriers, small polarons, are transferred to band states by either impact ionization or by tunneling. Such process would produce a huge conductivity increase and could be responsible for CCNDR. This hypothesis could explain the threshold switching in chalcogenides. It could be tested by high field transport measurements.

The current constriction due to CCNDR, in addition to the value in improving our understanding of resistive switching, has other important implications. One of them is a possibility of building extremely compact oscillators for applications in artificial neural networks.

6. In-situ electron microscopy

The physical changes that constitute the permanent filament have been assessed by the post mortem analysis of electro-formed and switched devices. The ex situ results obtained during this project and those by others are not conclusive with the primary difficulty being the small size of the filament. It is very easy to miss a 10 nm filament in a micron size device and focus on a feature that's not really relevant. In order to circumvent this difficulty, Carnegie Mellon University performed the electro-forming and switching *in situ* in the microscope column. Two types of samples were cut using Focused Ion Beam system. One was a single crystal rutile (TiO₂) with the surface protected during fibing by a sputtered layer of platinum. Pt was mechanically removed in the TEM with the help of nano-manipulator while the back contact was fabricated by deposition of tungsten layer by FIB. The second sample was also milled with the ion beam out of 20 nm Pt / 20 nm TiO₂ / 500 nm Pt / Si sputtered thin film structure. The schematic diagram of the experimental setup is shown in Fig. 20 with the sample welded by selective area deposition of tungsten to the STM tip and the other contact provided by the contact of the nano-manipulator with the top layer of the deposited structure. Such prepared switching devices exhibited standard switching *I-V* characteristics with the switching voltages of 2 - 4 V and dissipated power below 1 mW. Given the experimental setup it is clear that the TEM images capture the entirety of the changes in the device.

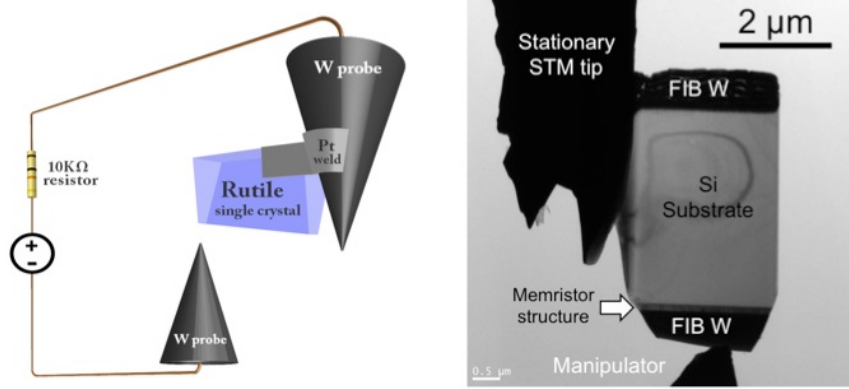


Fig. 20 (a) Schematic diagram of the *in-situ* TEM experiment. (b) Low magnification TEM image of the in situ thin film memristor sample with contacts.

The changes to the microstructure of the single crystal memristor are shown in Fig. 21. Fig. (d) and (h) show the bright field image and the diffraction pattern of the as-fabricated device. The contrast in the image is due to thickness fringes. The figures (e) through (k) correspond to increasing number of switching cycles. The progression of changes is apparent. The dark contrast appears in the upper left and lower left corners of the sample and occupies a progressively larger area with switching. The nature of the contrast can be identified by the changes in the diffraction pattern collected close to the lower left corner of the sample. In addition to the diffraction spots corresponding to perfect rutile crystal, one can see streaks increasing in intensity (i)-(j)-(k). The streaks correspond to formation of planar defects called Wadsley defects. Increasing intensity indicates increasing density of the faults. Eventually, the faults order into a new phase and the streaks convert into satellite diffraction spots. These observations agree reasonably well with the model proposed by Jeong *et al.* [18]. The important characteristics, however, are quite different. For one, there is no filament. Instead large fraction of the sample contains the Wadsley defects and as the consequence exhibits metallic conductivity.

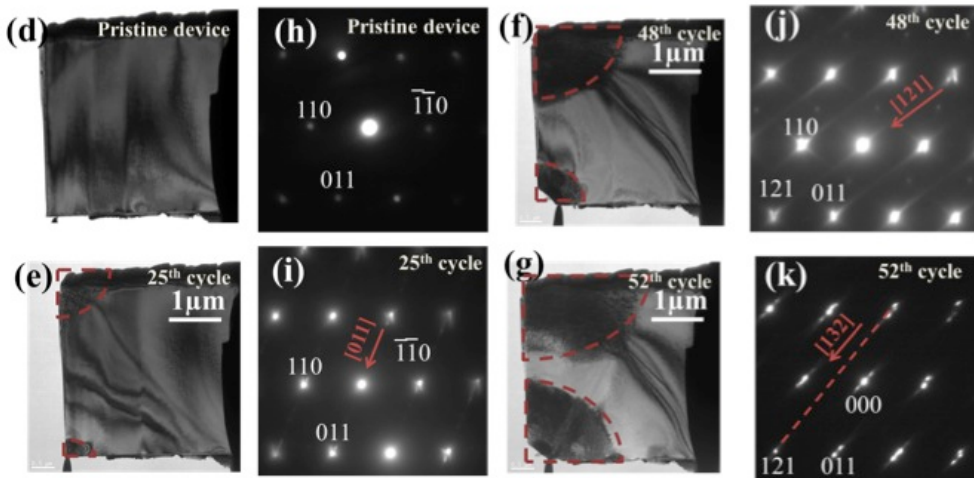


Fig. 21 (d), (e), (f), and (g) [1-11] bright field images of the as-fabricated TiO_2 specimen (c), and after 52 resistive switching cycles (e). Magneli phase areas are denoted by red dashed lines. (d) and (f) corresponding [1-11] selected area diffraction patterns obtained above W/ TiO_2 contact collected using a 500 nm diameter aperture.

The second unexpected result of the in situ experiment was obtained at the initial stages of switching. The pristine sample did not contain any extended defects as the dislocation density in bulk crystals is typically low. The sample switched without forming with the switching voltage about 2V (Fig. 22). The first three switching cycles (I-V characteristics of the third cycle is shown as the red trace) occurred without formation of ANY extended defects. The switching relied on point defects alone. Only with the increase of the dissipated power after the third cycle a small volume of Magneli phase appeared around the tungsten tip contact. This clearly contradicts the model and points to the role of point defects.

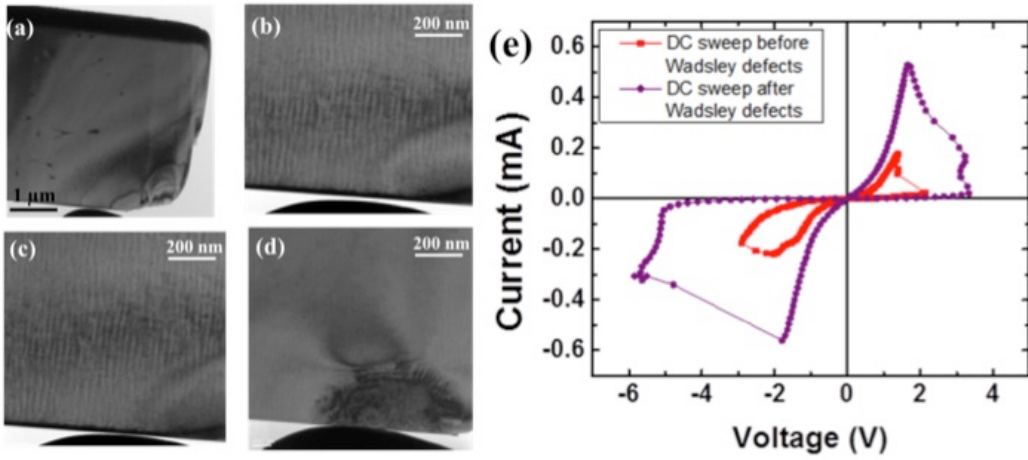


Fig. 22 TEM images on the left show (a) pristine sample, (b) and (c) the ON and OFF states in the first switching cycle, (d) the ON state during the fifth switching cycle and (e) the first and fifth switching cycle I-V characteristics.

The last noteworthy fact was the massive redistribution of Magneli phases after each switch between ON and OFF states. Most authors assumed that the second phase inclusions are essentially immobile with the changes, if any, occurring only at the very tip of the metallic filament only slightly modifying the width of the tunneling gap. The micrographs show quite the opposite (Fig. 23). The extent of the Wadsley defects changes by about a micron during a single switching cycle. Moreover it occurs discontinuously i.e. there is a gap of the material between the two regions of the Wadsley defects. In the SET process one of the regions grows while the other one is shrinking. During the RESET the regions switch their behavior. As the Wadsley defects are non-conservative i.e. the volume with Wadsley defects contains fewer oxygen atoms than the volume without them, the change in their spatial extent has to occur through the motion of oxygen ions. It also has to involve following steps: (i) separation of oxygen vacancies from the end of the planar fault, (ii) drift through the rutile crystal, and (iii) adsorption of the vacancy into another planar fault. The TEM observations prove that all of the above processes can occur during switching event and do occur to surprising extent.

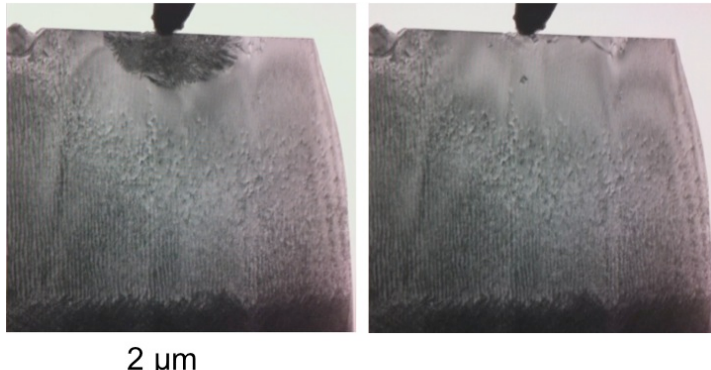


Fig. 23 Bright field images of the single crystal TiO_2 memristor in subsequent ON and OFF states. The images show massive redistribution of Magneli phases in each switching cycle from the proximity of the tungsten contact to the lower edge of the sample.

References:

- [1] R. Waser, R. Dittmann, G. Staikov, and K. Szot, *Adv. Mater* **21**, 2632 (2009).
- [2] W. Jiang, M. Noman, Y.M. Lu, J.A. Bain, S.P. A, and M. Skowronski, *J. Appl. Phys.* **110**, (2011).
- [3] Y.M. Lu, W. Jiang, M. Noman, J.A. Bain, P.A. Salvador, and M. Skowronski, *J Phys D Appl Phys* **44**, (2011).
- [4] K. Szot, W. Speier, G. Bihlmayer, and R. Waser, *Nat Mater* **5**, 312 (2006).
- [5] P. Gumbusch, S. Taeri-Baghbadrani, D. Brunner, W. Sigle, and A. Ruhle, *Phys Rev Lett* **87**, 085505 (2001).
- [6] K.-H. Yang, N.-J. Ho, and H.-Y. Lu, *J Am Ceram Soc* **94**, 3104 (2011).
- [7] Y.N. Picard, J.D. Caldwell, M.E. Twigg, C.R. Eddy, M.A. Mastro, R.L. Henry, R.T. Holm, P.G. Neudeck, A.J. Trunek, and J.A. Powell, *Appl. Phys. Lett.* **91**, 094106 (2007).
- [8] R.J. Kamaladasa, M. Noman, W. Chen, S.P. A, J.A. Bain, M. Skowronski, and Y.N. Picard, *J. Appl. Phys.* **113**, 234510 (2013).
- [9] D.-H. Kwon, K.M. Kim, J.H. Jang, J.M. Jeon, M.H. Lee, G.H. Kim, X.-S. Li, G.-S. Park, B. Lee, S. Han, M. Kim, and C.S. Hwang, *Nat Nanotechnol* **5**, 148 (2010).
- [10] J.P. Strachan, M.D. Pickett, J.J. Yang, S. Aloni, A.L.D. Kilcoyne, G. Medeiros-Ribeiro, and R.S. Williams, *Adv. Mater* **22**, 3573 (2010).
- [11] J.J. Yang, F. Miao, M.D. Pickett, D.A.A. Ohlberg, D.R. Stewart, C.N. Lau, and R. Stanley Williams, *Nanotechnology* **20**, 215201 (2009).
- [12] R. Muenstermann, J.J. Yang, J.P. Strachan, G. Medeiros-Ribeiro, R. Dittmann, and R. Waser, *Phys Status Solidi-R* **4**, 16 (2010).
- [13] J.P. Strachan, J.J. Yang, R. Muenstermann, A. Scholl, G. Medeiros-Ribeiro, D.R. Stewart, and R.S. Williams, *Nanotechnology* **20**, 485701 (2009).
- [14] F. Miao, J.P. Strachan, J.J. Yang, M.-X. Zhang, I. Goldfarb, A.C. Torrezan, P. Eschbach, R.D. Kelley, G. Medeiros-Ribeiro, and R.S. Williams, *Adv. Mater* **23**, 5633 (2011).
- [15] J.P. Strachan, G. Medeiros-Ribeiro, J.J. Yang, M.-X. Zhang, F. Miao, I. Goldfarb, M. Holt, V. Rose, and R.S. Williams, *Appl. Phys. Lett.* **98**, 242114 (2011).
- [16] Y.M. Lu, M. Noman, W. Chen, P.A. Salvador, J.A. Bain, and M. Skowronski, *J Phys D Appl Phys* **45**, 395101 (2012).
- [17] Y. Meng Lu, M. Noman, Y.N. Picard, J.A. Bain, P.A. Salvador, and M. Skowronski, *J. Appl. Phys.* **113**, 163703 (2013).
- [18] D.S. Jeong, H. Schroeder, U. Breuer, and R. Waser, *J. Appl. Phys.* **104**, 123716 (2008).
- [19] B.K. Ridley, *Proc. Phys. Soc.* **82**, 954 (1963).
- [20] A.F. Volkov and S.M. Kogan, *Sov. Phys. Usp.* **11**, 881 (1969).
- [21] S. Menzel, M. Waters, A. Marchewka, U. Böttger, R. Dittmann, and R. Waser, *Adv. Funct. Mater.* **21**, 4487 (2011).
- [22] M. Noman, A.A. Sharma, Y. Meng Lu, M. Skowronski, P.A. Salvador, and J.A. Bain, *Appl. Phys. Lett.* **102**, 023507 (2013).
- [23] T.E. Kaplan, *Appl. Phys. Lett.* **19**, 418 (1971).
- [24] T. Kaplan and D. Adler, *J. Non-Cryst. Solids* **8-10**, 538 (1972).
- [25] D. Adler, H.K. Henisch, and N. Mott, *Rev Mod Phys* **50**, 209 (1978).
- [26] D. Adler, M.S. Shur, M. Silver, and S.R. Ovshinsky, *J. Appl. Phys.* **51**, 3289 (1980).
- [27] K.L. Chopra, *J. Appl. Phys.* **36**, 184 (1965).
- [28] F. De Stefano, M. Houssa, V.V. Afanas'ev, J.A. Kittl, M. Jurczak, and A. Stesmans, *Thin Solid Films* **533**, 15 (2013).
- [29] M.D. Pickett, J. Borghetti, J.J. Yang, G. Medeiros-Ribeiro, and R.S. Williams, *Adv. Mater* **23**, 1730 (2011).
- [30] A.S. Alexandrov, A.M. Bratkovsky, B. Bridle, S.E. Savel'ev, D.B. Strukov, and R. Stanley Williams,

Appl. Phys. Lett. **99**, 202104 (2011).

- [31] D. Emin, Phys Today **35**, 34 (1982).
- [32] D. Emin and T. Holstein, Phys Rev Lett **36**, 323 (1976).
- [33] D. Emin, Phys. Rev. B **4**, 3639 (1971).
- [34] A. Janotti, C. Franchini, J.B. Varley, G. Kresse, and C.G. Van De Walle, Phys. Status Solidi RRL **7**, 199 (2013).